Lanzano, G., D'Amico, M., Felicetta, C., Puglia, R., Luzi, L., Pacor, F., Bindi, D. (2016): Ground-Motion Prediction Equations for Region-Specific Probabilistic Seismic-Hazard Analysis. - *Bulletin of the Seismological Society of America*,*106*, 1, pp. 73–92.

DOI: http://doi.org/10.1785/0120150096

THE SEISMOLOGICAL SOCIETY OF AMERICA
400 Evelyn Ave., Suite 201
Albany, CA 94706-1375
(510) 525-5474; FAX (510) 525-7204
www.seismosoc.org

Bulletin of the Seismological Society of America, Vol. 106, No. 1, pp. 73–92, February 2016, doi: 10.1785/0120150096

Ground-Motion Prediction Equations for Region-Specific Probabilistic Seismic-Hazard Analysis

by G. Lanzano, M. D'Amico, C. Felicetta, R. Puglia, L. Luzi, F. Pacor, and D. Bindi

Abstract The goal of this article is to investigate the possibility of reducing the uncertainty of the ground motion predicted for a specific target area (Po Plain and northeastern Italy), by calibrating a set of *ad hoc* ground-motion prediction equations (GMPEs). The derived GMPEs account for peculiarities that are not generally considered by standard predictive models, such as (1) an attenuation rate dependent on distance ranges and geological domains; (2) enhancement of short-period spectral ordinates, due to the reflection of *S* waves at the Moho discontinuity; and (3) generation of surface waves inside an alluvial basin.

The analyzed strong-motion dataset was compiled by selecting events in the 4.0–6.4 magnitude range, records with distances shorter than 200 km, and focal depths shallower than 30 km; the major contribution comes from the recent 2012 Emilia sequence (first mainshock, 20 May 2012 M_w 6.1; second mainshock, 29 May 2015 M_w 6.0). The GMPEs are derived for the geometrical mean of horizontal components of peak ground acceleration, peak ground velocity, and 5% damped spectral acceleration in the 0.04–4 s period range.

The derived region-specific models led to a reduction of the hazard levels for several intensity measures, with respect to the values obtained by considering the reference Italian attenuation model (Bindi *et al.*, 2011), as exemplified by the comparison of the hazard curves computed for two specific sites.

Online Material: Database of Northern Italy (DBNI) flat-file and tables of northern Italy ground-motion prediction equations (GMPEs) (NI15) regression coefficients and variability components for use with Joyner–Boore and hypocentral distances.

Introduction

The objective of probabilistic seismic-hazard analysis (PSHA) is the evaluation of the annual rate of exceedance of specified ground-motion levels at selected sites. The PSHA can be computed for the different intensity measures (IMs) generally used to represent the ground motion, such as the peak ground acceleration (PGA), peak ground velocity (PGV), and spectral acceleration (SA) for different periods and damping. For any scenario given in terms of magnitude, distance from the source, site conditions, and sometimes other variables, the probability distribution of the ground-motion intensity at the site is computed through ground-motion prediction equations (GMPEs). Most of the GMPEs have been derived using observed data from multiple stations and seismic sources. This has led to the compilation of global or multiregion flat files (e.g., Akkar *et al.*, 2013; Seyhan *et al.*, 2014). Global flat files have been significantly improved in terms of metadata related to stations (e.g., shear-wave velocities, depth to bedrock, basin effects) and earthquakes (e.g., style of faulting, source geometries), allowing us to increase the complexity of the models with the aim of reducing the epistemic uncertainty (e.g., Next Generation Attenuation-West 2; Boore *et al.*, 2014; Campbell and Bozorgnia, 2014).

Unfortunately, the large amount of data available for specific regions, especially after the occurrence of seismic sequences, does not necessarily reflect the completeness of information for the application of complex models. In addition, regions exist with specific source-to-site propagation settings that require the correct determination of the median values (Morikawa *et al.*, 2008; Lin *et al.*, 2011; Bradley, 2013). This is the case for ground motions recorded within and in the proximity of large alluvial basins, with very specific propagation effects and site response. Those settings are relevant, because they represent the typical configuration of large urban settings, which are usually located on large alluvial plains and exposed to high risk due to the presence

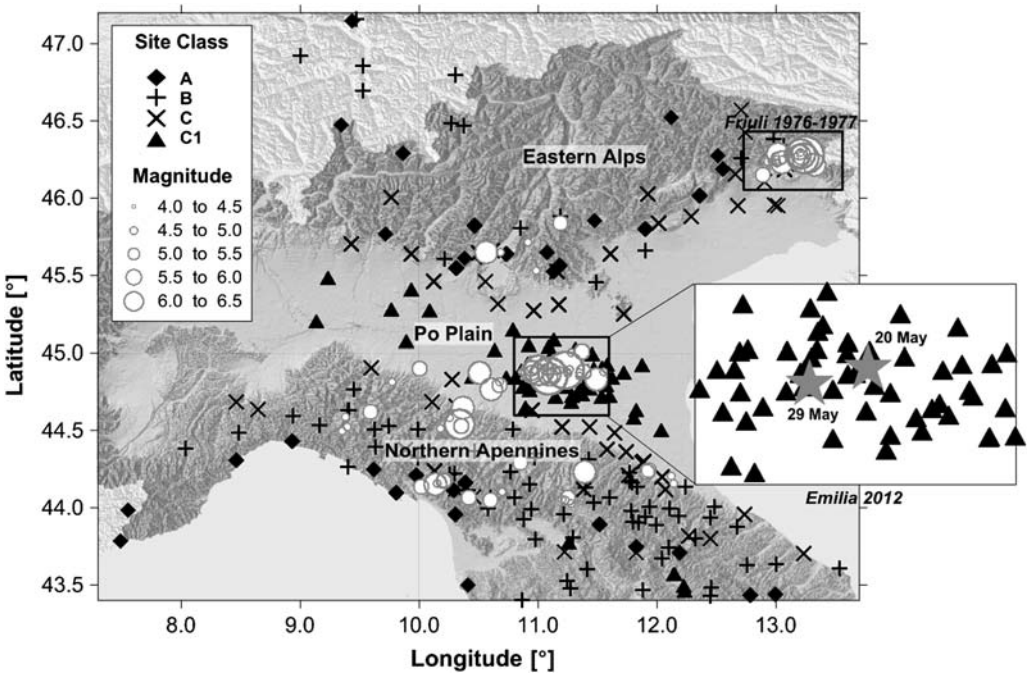

Figure 1. Geographic distribution of seismic events and recording stations of the Database of Northern Italy (DBNI). The two boxes represent the epicentral areas of the 1976–1977 Friuli and 2012 Emilia sequences, respectively.

of relevant lifelines, facilities, and infrastructures (e.g., Mexico City, Tehran, Los Angeles, and the Kanto basin, among others).

In this study, we consider an area including one of the largest alluvial basins in Europe (i.e., the Po Plain area, northern Italy), where the estimated seismic hazard is moderate (Stucchi *et al.*, 2011; Meletti *et al.*, 2012) but associated with a high level of exposure due to the large concentration of industries and infrastructures.

Recent studies have highlighted features of ground-motion characterization (GMC) that are specific for northern Italy. Bragato *et al.* (2011) observed that PGA is systematically enhanced at distances between 70 and 200 km, due to the effect of the reflection of *S* waves at the Moho discontinuity (*SmS* phase). Luzi *et al.* (2013) found that, in the Po Plain, the trapping and conversion of the body waves in the thick sedimentary cover causes the generation of surface waves, which dominate the seismic signals at periods longer than 2 s for the horizontal and vertical components. Besides the regional propagation effects, the local site effects are also extremely variable in the area, as observed by Castro *et al.* (2013) from the generalized inversion of Fourier spectral ordinates and by Bordoni *et al.* (2012) from the horizontal-to-vertical (H/V) spectral ratios computed considering the seismic records of the 2012 Emilia seismic sequence at several stations in the near-source region.

In this work, we test the performance of different ground-motion models (global, pan-European, and regional or local), highlighting their limits to predict the median ground-motion values for northern Italy, and we develop new GMPEs capable of describing the main features about site effects and wave propagation. Finally, we show that the tailored models can significantly improve the IMs' median estimates, leading to relevant changes in the PSHA compared with the reference Italian GMPEs (Bindi *et al.*, 2011).

Strong-Motion Dataset

We construct a dataset (database of Northern Italy [DBNI]) of records relative to earthquakes that occurred in a spatial window defined by the latitude range 44.0°–46.3° N and longitude range 8.00°–13.5° E. The dataset, composed of 2489 records relative to 300 stations and 94 events, was extracted from the ITalian ACcelerometric Archive (ITACA) 2.0 (Luzi *et al.*, 2008; Pacor *et al.*, 2011) according to the following criteria: (1) magnitude (M_w or M_L) larger than 4.0, (2) distance (R_{JB} or R_{epi}) in the 0–200 km range, and (3) event depth shallower than 30 km. Ⓔ The DBNI flat file (Table S1) is available in the electronic supplement to this article.

The majority of strong-motion data have been recorded by permanent and temporary accelerometers of the national accelerometric network (Rete Accelerometrica Nazionale [RAN]), operated by the Italian department of the civil protection (Dipartimento della Protezione Civile [DPC]), and by the network belonging to the Istituto Nazionale di Geofisica e Vulcanologia (INGV). A small percentage of records (3%) come from other Italian, French, and Swiss networks.

Figure 1 shows the study area and the geographic distribution of seismic events and recording stations. Two main seismic sequences are included in the dataset: the M_w 6.4 Friuli 1976–1977 and the M_w 6.1 Emilia 2012 sequences, both characterized by the reverse style of faulting. In

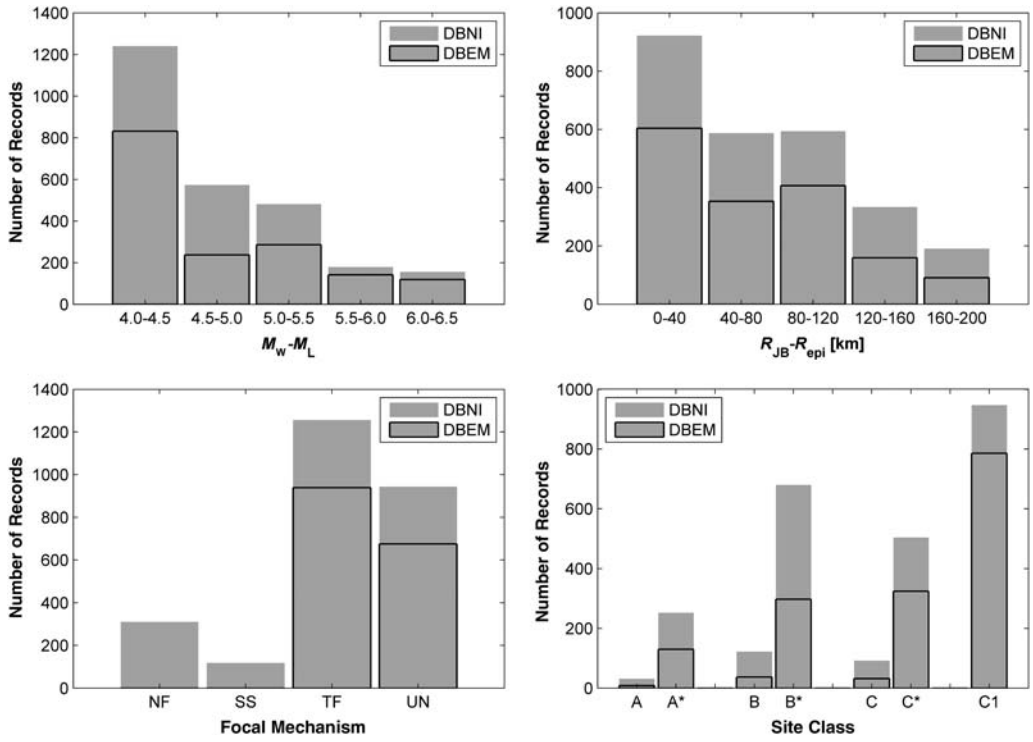

Figure 2. Distribution of the DBNI records; (top left) M_w or M_L; (top right) R_{JB} or R_{epi} distance (km); (bottom left) focal mechanism (NF, normal fault; SS, strike-slip fault; TF, thrust fault; UN, unknown); (bottom right) Eurocode 8 (EC8) site classes. Classes denoted with an asterisk lack shear-wave velocity profiles and have been classified according to the available geological information (Di Capua *et al.*, 2011). C1 identifies class C sites located within the alluvial basins. Black lines mark the contribution of the 2012 Emilia sequence (referred to as DBEM).

particular, about one-third of the events belong to the recent 2012 Emilia sequence (60% of records of DBNI).

The stations distribution is uniform in the northern Apennines (NA), eastern Alps, and central Po Plain, whereas there is a low station density in the western Alps and western Po Plain. DBNI includes 2489 waveforms of 94 events, recorded by 300 stations. Figure 2 shows the distributions of magnitude, distance, focal mechanisms, and Eurocode 8 (2004; EC8) site classes of the DBNI and the contribution of the 2012 Emilia sequence. The recording sites have been classified into three EC8 categories (A, B, and C), either on the basis of the average shear-wave velocity of the uppermost 30 m (V_{S30}) or of available geological information (Di Capua *et al.*, 2011). In the latter case, the site classes are indicated with an asterisk (i.e., A*, B*, and C*). Figure 3a,b shows the magnitude versus distance distribution and the distance distribution for each site class, respectively. Stations belonging to class C (i.e., V_{S30} between 180 and 360 m/s), located in the deepest part of the Po Plain or in smaller basins in the Apennines, have been isolated and grouped into a new site class named C1. The rationale for the modification of the site classification is that, for C1, complex 2D and 3D site effects are expected due to the presence of surface waves generated at the basin edges, with remarkable soil amplification at frequencies smaller than 1 Hz. Because one-third of the DBNI events are generated below the Po Plain, recordings at short distances are mainly associated with sites C and C1 (Fig. 3b).

In general, the events occurred in shallower crust (5–10 km) and are characterized by moderate magnitudes. About 10% of the records were recorded in the near fault (1–10 km) from temporary networks installed to record the aftershocks of the 2012 Emilia sequence. Thrust fault mechanisms are predominant (47.8%), while the percentage of normal (NF) and strike-slip (SS) mechanisms is 11.8% and 4.5%, respectively; the records characterized by undefined style of faulting (35.9%) come from events with magnitudes lower than 5.0.

The waveforms have been processed uniformly, according to the procedure described in Paolucci *et al.* (2011), which prescribes the application of a second-order acausal time-domain Butterworth filter to the zero-padded acceleration time series and zero-pad removal to make acceleration and displacement consistent after double integration. The typical band-pass frequency range is between 0.1 and 40 Hz for digital records, whereas it is narrower for analog ones (on average 0.3–25 Hz). Spectral ordinates used for the analysis are selected only within the usable frequency band, defined by the band-pass frequencies. This implies the reduction of about 5% and 8% of records for periods longer than 1 s and shorter than 0.07 s, respectively.

Table 1
Characteristics and Log-Likelihood (LLH) Ranking of the Candidate Ground-Motion Prediction Equations (GMPEs)

Model*	Region	Magnitude Type†	Magnitude	Period (s)	Distance Type	Distance (km)	Site Condition‡	Style of Faulting§	Depth (km)	IMs‖	Component#	LLH
BSSA14	Global	M_w	3.0–8.5	0.01–10	Joyner–Boore	0–400	V_{S30}	N, R/T, S, U	0–30	PGA, PGV, PSA	RotD50	0.96
CZ14	Global	M_w	4.5–7.9	0–10	Rupture	0–150	EC8 class/V_{S30}	N, R, S, U	0–23	PGA, PGV, DRS	GEOH	0.96
BND14	Pan-European	M_w–M_L	4.0–7.6	0.02–3	Joyner–Boore/Epicentral	0–300	EC8 class	N, R/T, S, U	0–35	PGA, PGV, PSA	GEOH	0.97
ITA10	Italian	M_w–M_L	4.0–6.9	0.04–2	Joyner–Boore/Epicentral	0–200	EC8 class	N, R/T, S, U	0–29	PGA, PGV, PSA	GEOH, Z	0.68
MS08	Local (NE Italy)	M_w–M_L	4.0–6.4	0.04–2	Epicentral	0–100	EC8 class	—	0–60	PGA, PGV, PSA, PSV, I_A, I_H, DV	H, Z	1.46

*BSSA14, Boore *et al.* (2014); CZ14, Cauzzi *et al.* (2014); BND14, Bindi *et al.* (2014); ITA10, Bindi *et al.* (2011); MS08, Massa *et al.* (2008).
†M_w, moment magnitude; M_L, local magnitude.
‡Eurocode 8 (EC8) class, definition of site class based on EC8 code (2004); V_{S30}, direct use of the shear velocity averaged over the upper 30 m in the equation.
§N, normal fault; R, reverse fault; T, thrust fault; S, strike fault; U, Unknown.
‖IM, intensity measure; PGA, peak ground acceleration; PGV, peak ground velocity; PSA, pseudospectral acceleration; PSV, pseudospectral velocity; I_A, Arias intensity; I_H, Housner intensity; DV, strong-motion duration.
#RotD50, median single-component horizontal ground motion across all nonredundant azimuths; GEOH, geometric mean of horizontal components; H, maximum amplitude of horizontal components; Z, vertical component.

Applicability of Existing Models

In this section, a selection of existing empirical models (global, pan-European, regional, or local) for ground-motion prediction are tested and discussed to highlight the applicability limits in the target area. The log-likelihood (LLH) method proposed by Scherbaum *et al.* (2009) is used to test the relative performance of different models against recorded data. Data-driven model selection potentially reduces epistemic uncertainties in GMC by reducing subjectivity and guiding the selection process in a quantitative and fully reproducible way (Delavaud *et al.*, 2009; Scherbaum *et al.*, 2009). The method, based on information theory, evaluates the probability for an observed ground-motion model to be realized under the hypothesis that an empirical model is true (Delavaud *et al.*, 2009; Beauval *et al.*, 2012). The negative average sample LLH (equation 1) measures the distance between a model and the data-generating distribution as

$$\mathrm{LLH}(g,x) = -\frac{1}{N}\sum_{i=1}^{N}\log_2[g(x_i)], \tag{1}$$

in which N is the number of observations x_i, and $g(x_i)$ is the probability density function (PDF) that model g has produced the observation x_i. A small LLH indicates that the candidate GMPEs are close to the model that has generated the data, whereas a large LLH corresponds to a model that is less likely to having generated the data.

Five models have been selected for the ranking:

- CZ14 (Cauzzi *et al.*, 2014) and BSSA14 (Boore *et al.*, 2014), both calibrated over global datasets;
- BND14 (Bindi *et al.*, 2014) calibrated over a pan-European dataset;
- ITA10 (Bindi *et al.*, 2011) derived from a set of Italian data (1972–2009); and
- MS08 (Massa *et al.*, 2008) derived from a local dataset recorded in northern Italy (1976–2008).

This selection updates the results of a previous study (Pacor *et al.*, 2012) carried out within the SeIsmic Ground Motion Assessment (SIGMA) project, which assessed the probabilistic seismic hazard at three sites in northern Italy. In particular:

- CZ14 supersedes Cauzzi and Faccioli (2008),
- BND14 supersedes Akkar and Bommer (2010), and
- BSSA14 supersedes the modified Atkinson and Boore (2011).

ITA10 and MS08 still represent the most updated regional and local models, respectively.

The main characteristics of each GMPE are listed in Table 1. The candidate GMPEs are heterogeneous in terms of magnitude, distance, and site condition; therefore, the test has been conducted using the appropriate variables and considering the range of validity of the candidate GMPEs (Table 1). The functional form of BSSA14 cannot be fully

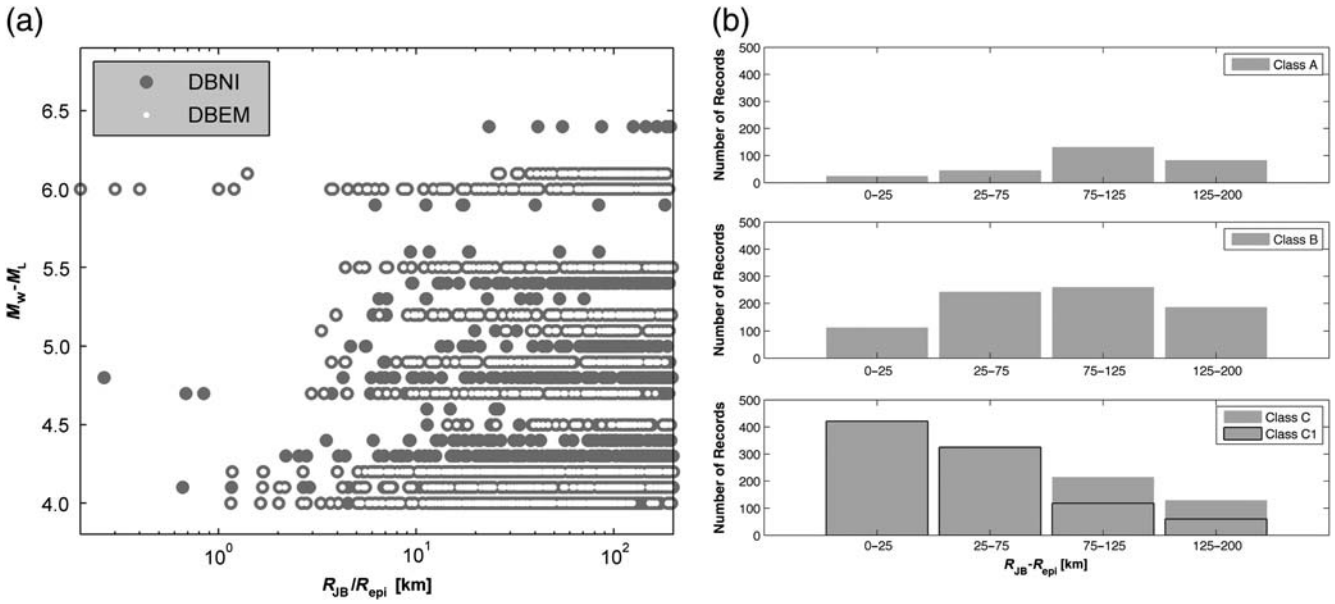

Figure 3. (a) Magnitude–distance distribution of the northern Italy dataset (DBNI). White dots highlight the contribution of the 2012 Emilia sequence (DBEM); (b) distance distribution of the records for each site class. Black lines mark the contribution of C1.

applied because of the lack of basin depths and shear-wave velocities for all sites. When unavailable, V_{S30} is approximated as follows: 800 m/s for A sites, 580 m/s for B sites, and 270 m/s for C/C1 sites, corresponding to the central value of the EC8 V_{S30} interval; the basin depth correction is set to zero, as recommended by Boore *et al.* (2014).

The LLH parameter has been calculated for 24 spectral periods between 0.04 and 2 s, as in ITA10 (Fig. 4a). Each period, defined in the five candidate GMPEs, is associated with the closest periods of ITA10, using a tolerance of ±0.015 s. Table 1 reports the average value of LLH calculated on the 24 periods.

The GMPE calibrated for Italy (ITA10, Bindi *et al.*, 2011) shows the best fit to the data compared with global or pan-European models, especially at short periods. The MS08 GMPEs show a poor fit, although calibrated on a dataset recorded in the same area (period 1976–2008). The main causes of the GMPEs failure are (1) limited amount of data (mainly low-magnitude events); (2) poor quality of event metadata (e.g., moment magnitude obtained by the conversion of local magnitude); (3) simplified site classification, which includes only two site categories, identified on the basis of H/V spectral ratio; and (4) use of epicentral distance.

We perform additional analyses to disaggregate, over the period–distance domain, both the LLH values and the total residuals R_{es} (evaluated as the logarithm of the ratio between observations and prediction) for ITA10. Figure 4b highlights that ITA10 cannot fully capture the ground-motion features at short periods (0.05–0.25 s) and distances larger than 30 km. In particular, the residuals plotted in Figure 4c show that ITA10 overestimates the observed ground motion, especially in the 30–60 km distance range, at periods shorter than 0.3 s. Conversely, positive residuals are observed at long period and short distances (< 20 km). Figure 4d–f shows additional information on residuals, in particular the standard deviation associated with short (0.15 s), intermediate (1 s), and long periods (2 s). The largest standard deviations are observed for short periods (0.15 s) and large distances (> 70 km).

These results suggest that the model by Bindi *et al.* (2011) does not include all physical factors controlling the ground motion in the study area, such as specific propagation effects or site amplifications or deamplifications, due to the effect of the thick sedimentary cover of the Po Plain.

High- and Low-Frequency Ground-Motion Features

Figure 5a displays the location of stations with distances larger than 50 km from the epicenter of the second mainshock of the 2012 Emilia sequence, and Figure 5b shows the PGA decay with distance. We can observe that the PGA recorded by stations located to the north of the Po Plain is 3–5 times larger than the PGA recorded to the south. This phenomenon has been already observed by Douglas *et al.* (2004) in central Italy and southern Iceland and by Bragato *et al.* (2011) in northern Italy and is explained as the enhancement of ground motion due to *S*-wave reflection at the Moho discontinuity (*SmS* phase).

In particular, Bragato *et al.* (2011) investigated the ground-motion characteristics using two datasets: the first composed of waveforms of the 2008 M_L 5.2 Parma and small-magnitude earthquakes of the 1976 Friuli seismic sequence and the second composed of macroseismic intensity points in northern Italy, converted in PGA, using the Faenza and Michelini (2010) empirical relation. Bragato *et al.* clearly

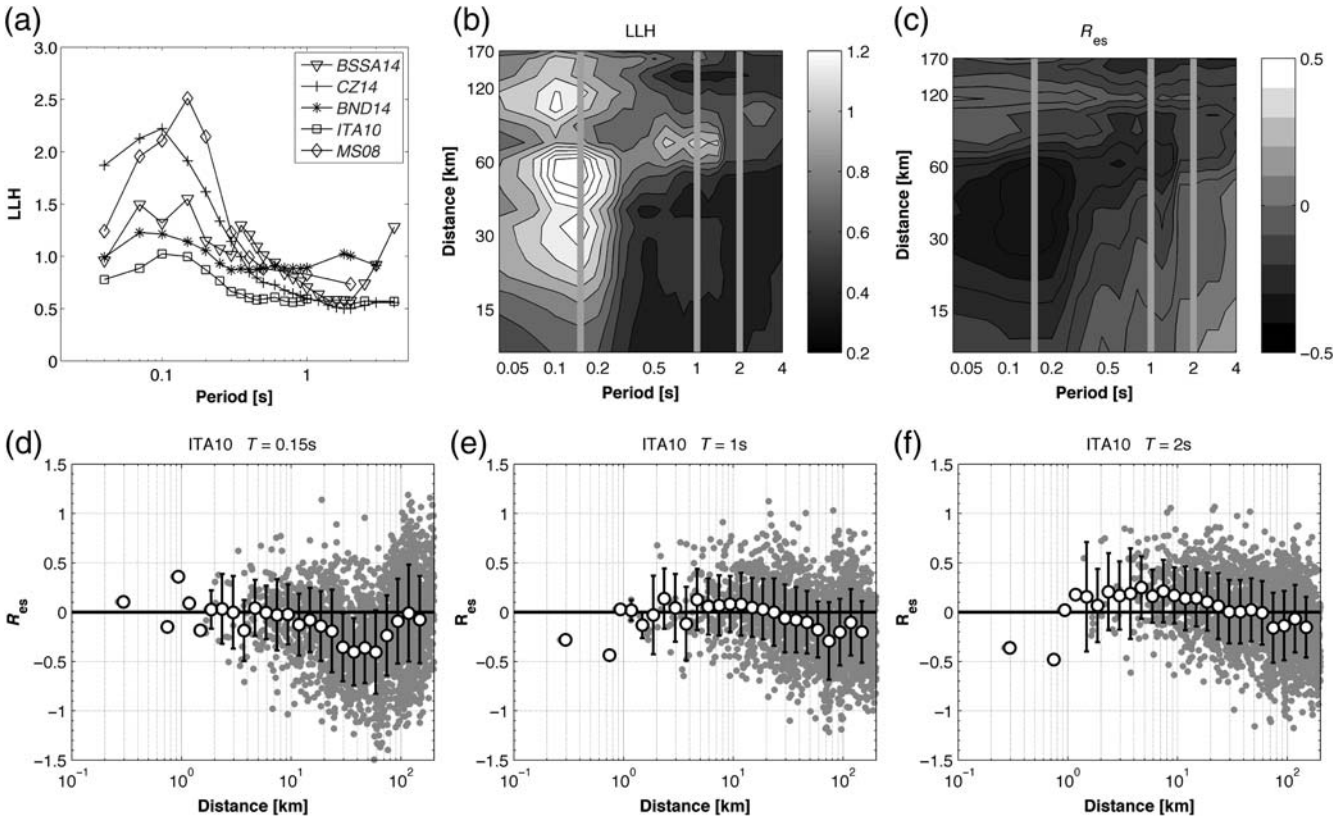

Figure 4. (a) Log-likelihood (LLH) trend for the five candidate ground-motion prediction equations (GMPEs) versus period (CZ14, Cauzzi *et al.*, 2014; BSSA14, Boore *et al.*, 2014; BND14, Bindi *et al.*, 2014; ITA10, Bindi *et al.*, 2011; and MS08, Massa *et al.*, 2008); (b) disaggregation of LLH values for ITA10 in terms of distance and period; (c) disaggregation of ITA10 total residuals (R_{es}) in terms of distance and period; and (d)–(f) ITA10 total residuals in function of distance at 0.15, 1, and 2 s. White dots and black bars represent the mean value and standard deviation of the residuals for each distance bin, respectively.

recognized the enhancement of PGA around 50 km due to the Moho reflection from both datasets (their figs. 8 and 11).

Figure 5c,d displays the acceleration time histories of the second Emilia shock normalized by their peak amplitudes and filtered in the 3–10 Hz frequency range to highlight the arrivals of direct *S* and *SmS* phases.

Figure 6 displays the acceleration transversal components and their instantaneous Fourier transforms, for pairs of stations at the same epicentral distance, located either in the Po Plain and eastern Alps (PEA) or in the NA. We can observe that the energy of PEA records is concentrated in short time intervals, after the *S*-wave arrivals and in the 3–10 Hz frequency range, whereas records in the NA are characterized by longer duration and scattered energy release at lower frequencies (<5 Hz).

The crustal structure of the PEA region is relatively simple, because the top of the Mesozoic limestone forms a regional monocline dipping to the south underneath the NA thrust front (Fig. 7). This geological setting can produce the large-amplitude reflection from the Moho (Fig. 5c) because there is little interaction of phases with other crustal features. As the geologic structure becomes complex, such as in the NA front, the energy tends to be partitioned into more phases, so that the amplitude of *SmS* tends to become negligible (Fig. 5d).

Ground motion at low frequencies (<0.5 Hz) is dominated by surface waves, both for the horizontal and vertical components for sites located inside or outside the Po River basin. Figure 8 shows the radial and vertical components of velocity time histories recorded at four stations belonging to different site classes (A–C1) and the related instantaneous Fourier transforms. Surface waves cause the lengthening of the signal and large amplitudes at low frequencies, even for rock sites (station ASOL). In many cases, the peak amplitudes are observed on later phases, such in the case of ZCCA (epicentral distance of about 55 km), where PGV is observed at about 50 s, corresponding with surface-wave arrivals. In this case, the amplitudes of vertical and horizontal components are of the same order (Bordoni *et al.*, 2012; Luzi *et al.*, 2013; de Nardis *et al.*, 2014).

Calibration of Region-Specific GMPEs

The peculiarities observed in the previous section led us to derive a new set of prediction equations for the area (hereinafter NI15) to introduce the physical factors controlling the ground motion.

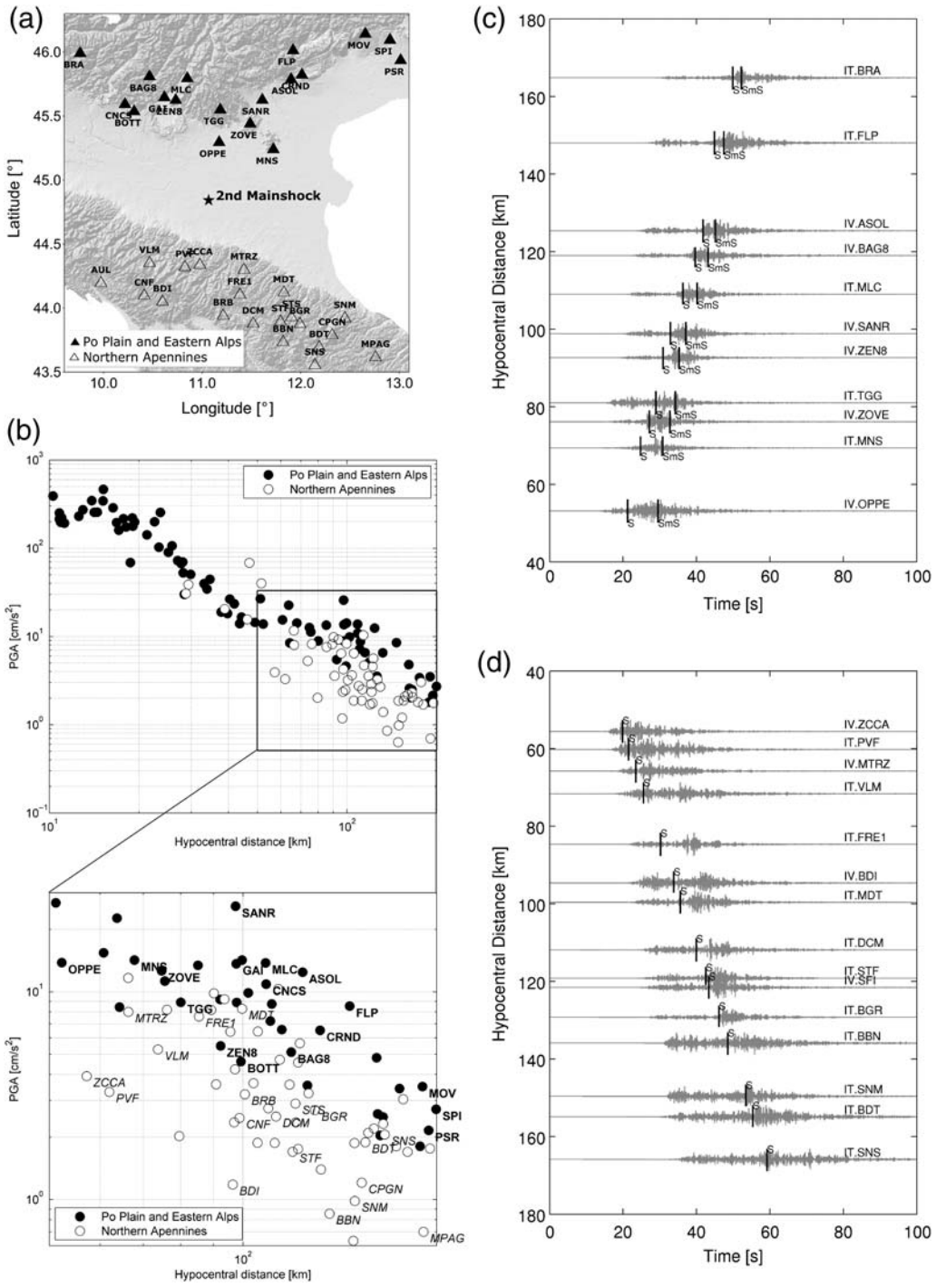

Figure 5. (a) Map of the stations located beyond 50 km from the epicenter of the second mainshock of the Emilia sequence (29 May 2012, 07:00:03); (b) acceleration time histories of the stations located in the Po Plain and eastern Alps (PEA); (c) observed peak ground acceleration (PGA) versus hypocentral distance; (d) acceleration time histories of the stations located in the northern Apennines (NA). The black lines identify the *S* waves or *SmS* arrivals. Because of visualization needs, waveforms are normalized by their peak amplitudes. The arrival times have been calculated with a simple 1D model hypothesizing a homogenous crustal layer down to 30 km and lateral increments of the *S*-wave velocity (2.5–3.3 km/s from the Po Plain to the Alps). A constant *S*-wave velocity of 2.8 km/s was used to characterize the crust below the Apennines.

We start from the same functional form used for ITA10 (Bindi *et al.*, 2011):

$$\log_{10} Y = a + F_M(M) + F_D(R, M) + F_{\text{sof}} + F_S + F_{\text{bas}}, \quad (2)$$

in which Y is the geometrical mean of the horizontal components (GEOH) of the following strong-motion parameters: PGA (expressed in cm/s^2), PGV (in cm/s), and 5% damped SA (in cm/s^2) computed over 24 periods in the 0.04–4 s range. The parameter a is the offset of the model, whereas

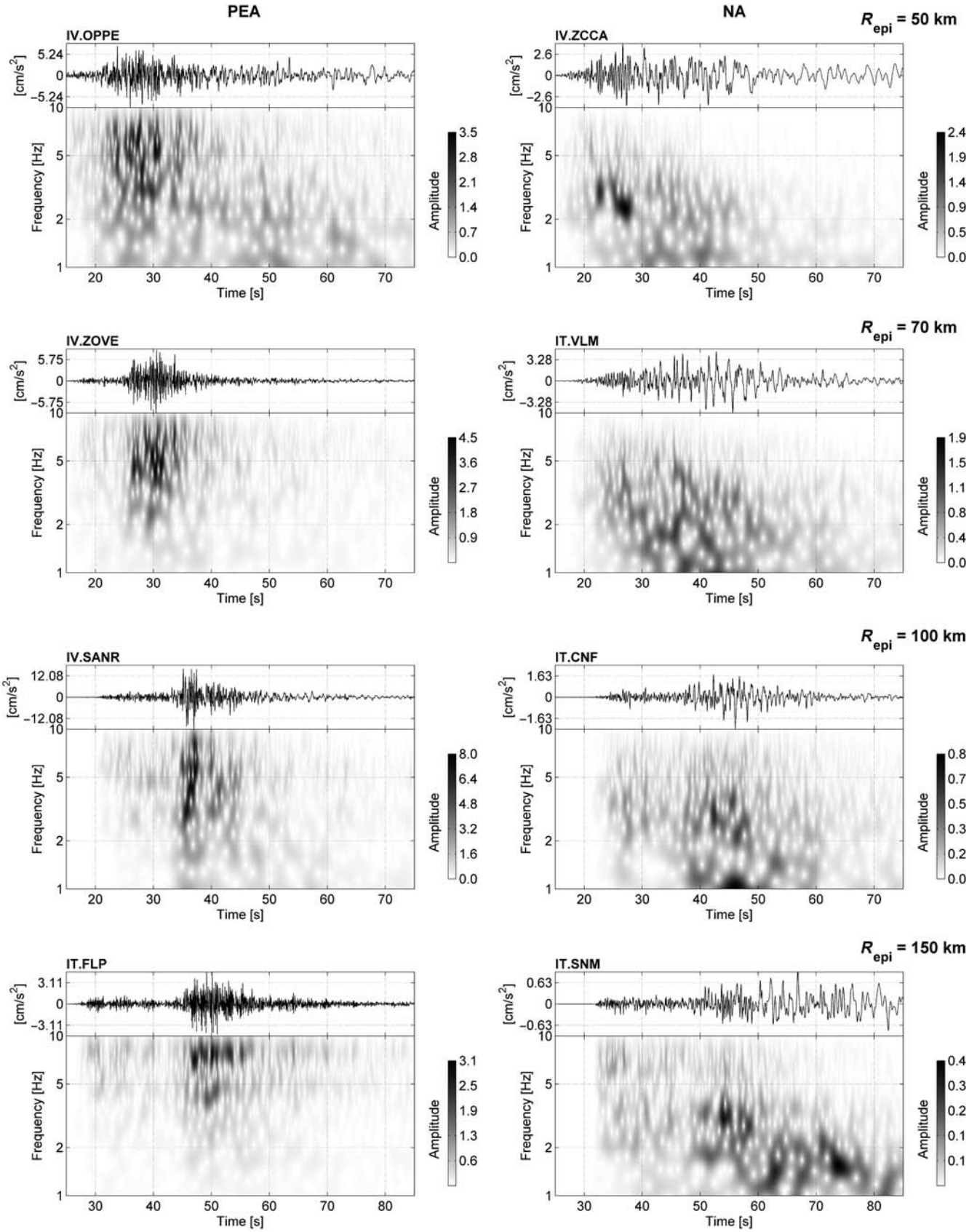

Figure 6. Instantaneous Fourier transform of the transversal component of acceleration, recorded by stations at distances farther than 50 km from the second mainshock of the Emilia sequence (29 May 2012 M_w 6.1, 07:00:03). (Left column) stations located in the PEA; (right column) stations located in the NA.

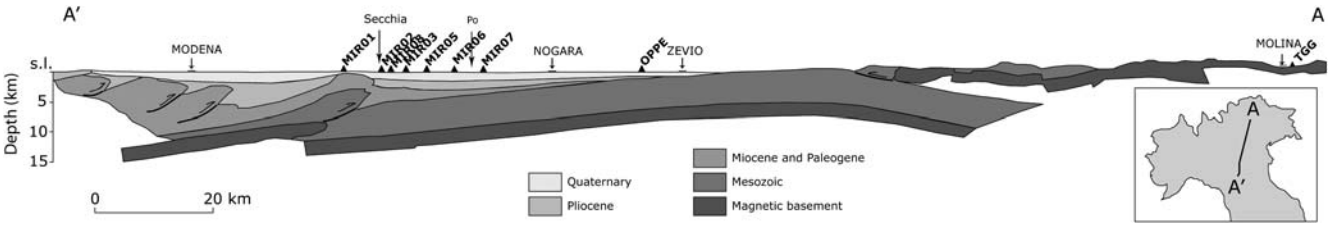

Figure 7. Geological cross section from NA to southeastern Alps (modified after Cassano *et al.*, 1986).

$F_D(R,M)$, $F_M(M)$, F_S, F_{sof}, and F_{bas} represent the distance function, the magnitude scaling, the site amplification, the style of faulting, and basin-effects correction, respectively; M is the magnitude (M_{w} or M_{L} in cases in which M_{w} is missing), and R (in km) is the distance. The equation for the distance function is

$$F_D(R,M) = [c_1 + c_2(M - M_r)]\log_{10}\left(\frac{R}{R_h}\right), \qquad (3)$$

in which c_1 and c_2 are the attenuation coefficients; M_r is a reference magnitude fixed to 5.0; R is either the hypocentral distance (R_{hypo}) or the distance computed as $\sqrt{R_{\text{JB}}^2 + h^2}$, in which R_{JB} is the Joyner–Boore distance and h is the pseudodepth coefficient; R_h is a hinge distance introduced to account for changes in the attenuation rate.

Because attenuation depends both on the geologic domain (i.e., PEA or NA) and distance ranges (Figs. 4 and 5), an index j is introduced, taking the following values:

1. sites located on PEA and $R \le R_h$,
2. sites located on PEA and $R > R_h$,
3. sites located on NA and $R \le R_h$, and
4. sites located on NA and $R > R_h$.

Therefore, equation (3) for the distance function $F_D(R,M)$ is modified as follows:

$$F_D(R,M) = [c_{1j} + c_{2j}(M - M_r)]\log_{10}\left(\frac{R}{R_h}\right)(j = 1,\ldots 4), \qquad (4)$$

in which R_h is set to 70 km, similarly to Castro *et al.* (2013) for the Po Plain area or Douglas *et al.* (2004) for central Italy and southern Iceland (see also Fig. 5b).

To distinguish among the sites located in PEA and NA, a geographic separation (depicted in Fig. 1) has been defined through the linear equation $\text{LAT}_{\text{ref}} = -0.33\text{LON}_{\text{s}} + 48.3$, in which LON_{s} is the station longitude and LAT_{ref} is the reference latitude, expressed in decimal degrees. Positive differences between station latitude LAT_{s} and LAT_{ref} identify the PEA sites, and negative differences identify the NA ones.

The magnitude function is given by

$$F_M(M) = b_1(M - M_r) + b_2(M - M_r)^2, \qquad (5)$$

in which M_r is the reference magnitude, defined in equation (3). The magnitude saturation has been not considered, because there is no evidence from the data.

The term F_{sof} in equation (2) represents the style of faulting correction and is given by

$$F_{\text{sof}} = f_j E_j (\text{with } j = \text{NF, TF, UN}), \qquad (6)$$

in which f_j are the coefficients to be determined during the analysis and E_j are dummy variables used to denote the different style of faulting: normal (NF), thrust (TF), and unspecified (UN). The few SS events have been discarded as not representative for the investigated area. The regression for the style of faulting model is performed while constraining the coefficient to zero for unspecified mechanism (reference style of faulting).

The term F_S in equation (2) represents the site amplification and is given by

$$F_S = s_j S_j (\text{with } j = \text{A, B, C}), \qquad (7)$$

in which s_j are the coefficients to be determined through the regression, whereas S_j are dummy variables used to denote the three EC8 site classes (A, B, and C). The regression is performed while constraining the coefficient for class A to zero (reference site class).

From the analysis of ITA10 residuals, the bias observed at short periods in the 30–100 km distance range (Fig. 4d) can be mainly ascribed to the station in class C, located within the Po basin (Fig. 3b). To capture this feature, an additional term has been introduced in the functional form. Hence, the basin-effect term in equation (2) is defined as

$$F_{\text{bas}} = \delta_{\text{bas}}\Delta_{\text{bas}}, \qquad (8)$$

in which δ_{bas} is the coefficient to be determined during the analysis and Δ_{bas} is the dummy variable, assuming a value of 1 for sites located in the middle of a basin and a value of 0 otherwise.

The regressions are performed applying the random effect approach (Abrahamson and Youngs, 1992) to determine the between-event (δB_e) and within-event (δW_{es}) components of total residuals (R_{es}), according to Al Atik *et al.* (2010). The NI15 coefficients and the standard deviation σ and its components (the between-event τ and within-event ϕ standard deviation) are shown in Tables 2–5 for Joyner–Boore distance. Ⓔ Analogous tables for hypocentral distance are available in the electronic supplement (Tables S2 and S3).

In Figures 9 and 10, the median prediction for the SA ordinates (periods 0.15, 1, and 2 s) over distance is compared

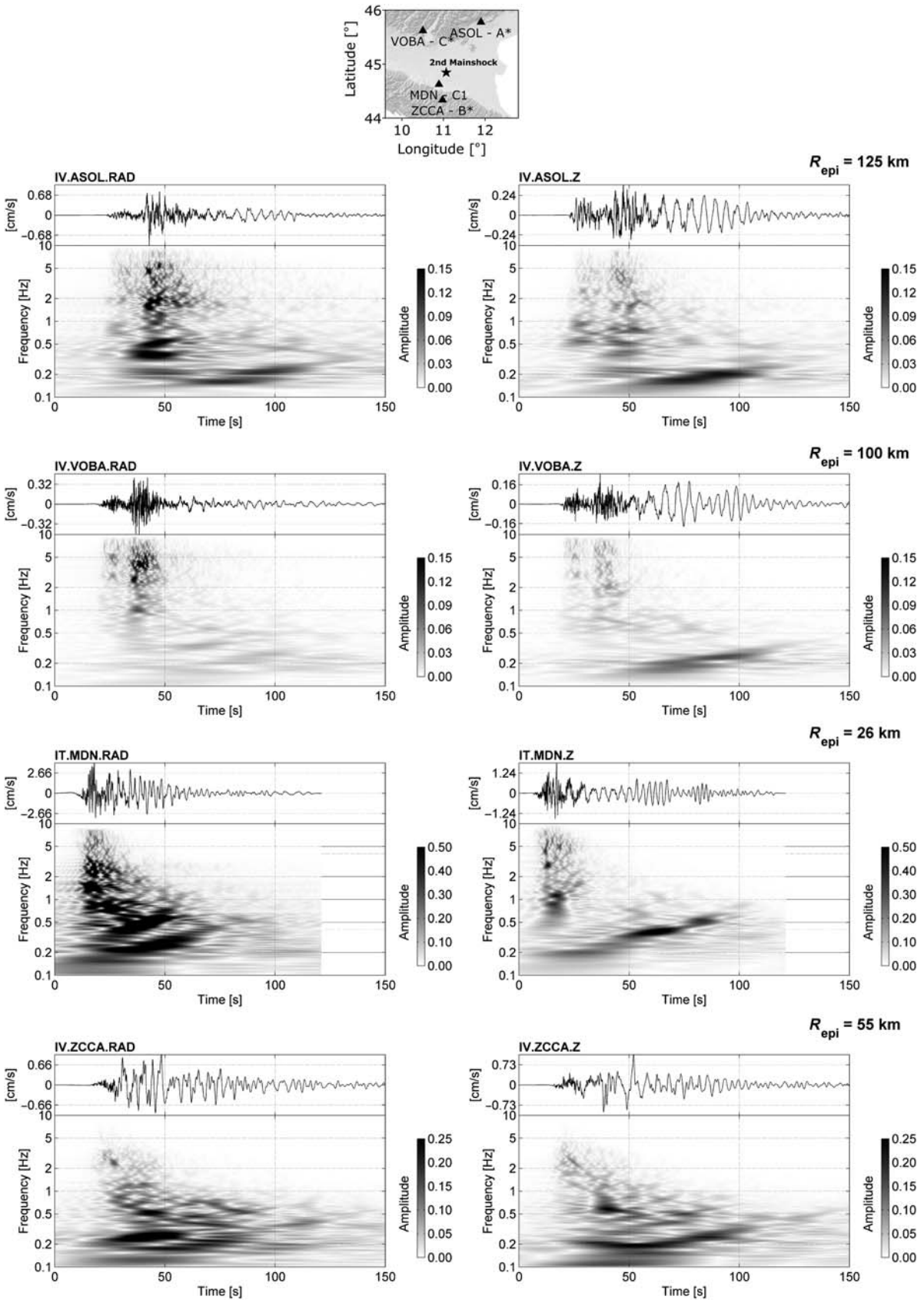

Figure 8. Instantaneous Fourier transform of the velocity time series for different stations and site classes (ASOL-A*, VOBA-C*, MDN-C1, and ZCCA-B*) recorded during the second mainshock of the Emilia sequence (29 May 2012 M_w 6.1, 07:00:03). (Left column) radial component; (right column) vertical component.

Table 2
Northern Italy (NI15) Regression Coefficients and Variability Components for GEOH of the Spectral Acceleration (SA) Ordinates (cm/s^2)

T (s)	a	b_1	b_2	c_{11}	c_{21}	c_{12}	c_{22}	c_{13}	c_{23}	c_{14}	c_{24}
0.04	0.122	0.565	−0.015	−1.967	0.305	−0.968	0.026	−1.872	0.567	−2.280	0.443
0.07	0.258	0.555	−0.017	−2.131	0.299	−0.885	0.087	−1.986	0.593	−2.501	0.486
0.1	0.334	0.537	−0.011	−2.125	0.268	−0.742	0.123	−1.996	0.486	−2.573	0.451
0.15	0.431	0.561	−0.008	−1.979	0.235	−0.804	0.070	−1.890	0.452	−2.443	0.348
0.2	0.436	0.579	−0.014	−1.847	0.201	−0.810	0.066	−1.820	0.348	−2.321	0.364
0.25	0.436	0.610	−0.020	−1.790	0.196	−0.905	0.022	−1.683	0.357	−2.205	0.311
0.3	0.394	0.629	−0.015	−1.759	0.180	−0.963	0.009	−1.639	0.305	−2.065	0.343
0.35	0.335	0.644	−0.008	−1.724	0.165	−1.009	0.015	−1.631	0.243	−1.979	0.328
0.4	0.284	0.662	−0.010	−1.662	0.155	−1.080	0.004	−1.641	0.182	−1.863	0.282
0.45	0.240	0.683	−0.010	−1.646	0.146	−1.045	−0.017	−1.648	0.169	−1.737	0.266
0.5	0.182	0.699	−0.009	−1.601	0.140	−1.027	−0.027	−1.638	0.166	−1.663	0.270
0.6	0.084	0.727	−0.017	−1.549	0.107	−0.963	0.000	−1.584	0.170	−1.492	0.244
0.7	0.010	0.751	−0.025	−1.509	0.091	−0.956	−0.001	−1.561	0.134	−1.373	0.209
0.8	−0.051	0.771	−0.034	−1.460	0.100	−0.989	0.028	−1.520	0.149	−1.307	0.225
0.9	−0.114	0.799	−0.036	−1.417	0.114	−0.985	0.016	−1.463	0.180	−1.212	0.259
1	−0.158	0.827	−0.043	−1.373	0.130	−1.009	0.000	−1.411	0.206	−1.189	0.207
1.2	−0.260	0.879	−0.041	−1.316	0.166	−1.038	−0.020	−1.313	0.267	−1.173	0.121
1.4	−0.323	0.909	−0.052	−1.264	0.157	−1.139	0.053	−1.208	0.260	−1.262	0.116
1.6	−0.409	0.946	−0.045	−1.238	0.150	−1.214	0.046	−1.128	0.323	−1.278	0.072
1.8	−0.486	0.977	−0.039	−1.218	0.141	−1.239	0.066	−1.103	0.313	−1.315	0.014
2	−0.554	0.997	−0.037	−1.189	0.138	−1.263	0.069	−1.100	0.282	−1.345	0.057
2.5	−0.742	1.034	−0.027	−1.164	0.151	−1.326	0.045	−1.072	0.299	−1.385	0.060
3	−0.881	1.057	−0.019	−1.152	0.165	−1.378	0.018	−1.020	0.339	−1.449	0.084
4	−1.084	1.134	0.019	−1.101	0.244	−1.488	−0.153	−0.971	0.414	−1.619	−0.119

Table 3
NI15 Regression Coefficients and Variability Components for GEOH of the SA Ordinates (cm/s^2)

T (s)	h (km)	f_{NF}	f_{TF}	s_B	s_C	δ_{bas}	τ	ϕ	σ
0.04	6.507	0.058	0.199	0.028	0.189	−0.094	0.108	0.324	0.342
0.07	7.296	0.042	0.182	−0.002	0.161	−0.099	0.113	0.340	0.359
0.1	7.463	0.032	0.193	0.018	0.180	−0.102	0.118	0.354	0.373
0.15	7.073	0.024	0.183	0.033	0.180	−0.081	0.118	0.353	0.372
0.2	6.698	0.022	0.191	0.058	0.209	−0.070	0.114	0.342	0.360
0.25	6.933	0.035	0.183	0.065	0.201	−0.029	0.110	0.331	0.349
0.3	7.016	0.038	0.177	0.075	0.219	−0.016	0.108	0.323	0.340
0.35	7.304	0.044	0.178	0.081	0.241	0.012	0.105	0.316	0.333
0.4	7.272	0.031	0.176	0.088	0.257	0.046	0.103	0.309	0.326
0.45	7.500	0.025	0.169	0.078	0.255	0.073	0.102	0.305	0.322
0.5	7.493	0.030	0.168	0.086	0.270	0.094	0.101	0.303	0.319
0.6	7.135	0.024	0.150	0.097	0.280	0.125	0.101	0.303	0.319
0.7	7.044	0.006	0.131	0.108	0.292	0.123	0.100	0.301	0.317
0.8	6.943	−0.004	0.122	0.104	0.292	0.123	0.101	0.302	0.318
0.9	6.760	−0.004	0.108	0.100	0.293	0.131	0.100	0.300	0.316
1	6.500	−0.003	0.098	0.091	0.289	0.136	0.100	0.300	0.316
1.2	6.026	0.004	0.091	0.087	0.289	0.131	0.100	0.299	0.315
1.4	5.366	−0.004	0.075	0.082	0.293	0.119	0.099	0.298	0.314
1.6	5.033	0.000	0.070	0.085	0.303	0.115	0.099	0.297	0.313
1.8	4.737	−0.001	0.067	0.080	0.303	0.119	0.100	0.299	0.315
2	4.241	−0.010	0.056	0.081	0.308	0.117	0.099	0.298	0.314
2.5	4.126	0.040	0.054	0.085	0.327	0.115	0.100	0.301	0.317
3	4.170	0.072	0.045	0.089	0.325	0.114	0.101	0.304	0.320
4	4.454	0.073	0.019	0.096	0.322	0.131	0.113	0.298	0.318

σ, total variability; τ, between-event variability; ϕ, within-event variability.

Table 4
NI15 Regression Coefficients and Variability Components for GEOH of PGA (cm/s^2) and PGV (cm/s^2)

IMs	a	b_1	b_2	c_{11}	c_{21}	c_{12}	c_{22}	c_{13}	c_{23}	c_{14}	c_{24}
PGA	0.071	0.603	−0.019	−1.895	0.286	−0.926	0.035	−1.838	0.511	−2.256	0.455
PGV	−1.142	0.767	−0.005	−1.623	0.230	−1.037	−0.054	−1.596	0.379	−1.741	0.348

Table 5
NI15 Regression Coefficients and Variability Components for GEOH of PGA (cm/s^2) and PGV (cm/s^2)

IMs	h (km)	f_{NF}	f_{TF}	s_B	s_C	δ_{bas}	τ	ϕ	σ
PGA	6.701	0.035	0.181	0.050	0.203	−0.060	0.106	0.318	0.336
PGV	5.904	0.022	0.144	0.085	0.260	0.037	0.096	0.288	0.304

σ, total variability; τ, between-event variability; ϕ, within-event variability.

to observations for thrust fault events having magnitude 4.5 or 6.0. Two sets of attenuation curves are displayed: the top panel in each pair refers to sites located in the PEA and the bottom panel refers to the NA sector. Figure 9 represents class B, and Figure 10 represents class C sites located inside sedimentary basins (C1).

The most striking result is the different attenuation trend at short periods (< 1 s), observed in the PEA and NA. In the northern sector, there is a significant change in the attenuation before and after the hinge distance (70 km), due to the Moho reflections. Conversely, in the southern sector the change in attenuation is negligible.

The trends of the site coefficients for NI15 and ITA10, class C, are shown in Figure 11 as a function of period. Sites located inside sedimentary basins (denoted with C1) show a very different trend compared to sites located outside such basins (class C). At short periods (< 0.4 s) the correction for basin effects gives coefficients about 1.3 times lower than ITA10 or NI15 (class C). This might be explained with a strong attenuation of short-period phases propagating through thick sedimentary covers. Conversely, at long periods (> 0.4 s), sites located inside sedimentary basins show an increase of amplification, up to 1.5 times compared to class C.

The total (σ) and the between-event (τ) and within-event (ϕ) standard deviations are plotted in Figure 12 as a function of period. The total variability of the DBNI residuals with respect to ITA10 was also added to demonstrate the decrease of uncertainty introducing the factors controlling the ground motion in the area (different attenuation models and basin effects). The reduction of the total variability is about 10%, especially observed at short periods. The between-event variability is almost constant (about 0.1), and the largest part of it is carried by the within-event residuals.

Figure 13 shows the distribution of residuals between observations and NI15 predictions at three selected periods (0.15, 1, and 2 s). Figure 13a shows the PDF of the NI15 residuals superimposed on the PDF and histogram of the ITA10 residuals. Figure 13b shows the distributions of the total residuals (R_{es}) as a function of distance. The biased trend of ITA10 residuals, observed in Figure 4d ($T = 0.15$ s, distance range 30–100 km), has been strongly reduced (Fig. 13b, left column) mainly because of the introduction of the basin effect term. At longer periods (1 and 2 s), there is an overall benefit over the entire distance range.

Hazard Assessment

To exemplify the impact of the derived GMPEs on the median hazard in the investigated area, the hazard curves for two sites are computed considering the GMPEs derived in this study (NI15) and the model proposed for Italy (ITA10). Figure 14 shows the seismic source zones of northern Italy used to derive the Italian hazard map (Meletti *et al.*, 2008) and the location of the two selected sites. The first one (site S1, class C) is located close to the Po basin edge, about 40 km north from the source area containing the Emilia sequence (seismic source zone 912 in Fig. 14). The second site (site S2, class C1) is located within the Po basin, inside zone 912.

Although the goal of the hazard computation is to compare the outcomes obtained with two different GMPEs, we use the same input parameters adopted for a branch of the logic tree used to calculate the Italian hazard map (Stucchi *et al.*, 2011) that considers the zonation proposed by Meletti *et al.* (2008), the truncated Gutenberg–Richter relationship to describe the mean annual rate of exceedance of earthquakes and the historical completeness of the Catalogo Parametrico dei Terremoti Italiani, versione 2004 (CPTI04) catalog (Stucchi *et al.*, 2011). Table 6 reports the input parameters for the hazard calculation. The computation has been carried out using CRISIS 2015 (Ordaz *et al.*, 2013).

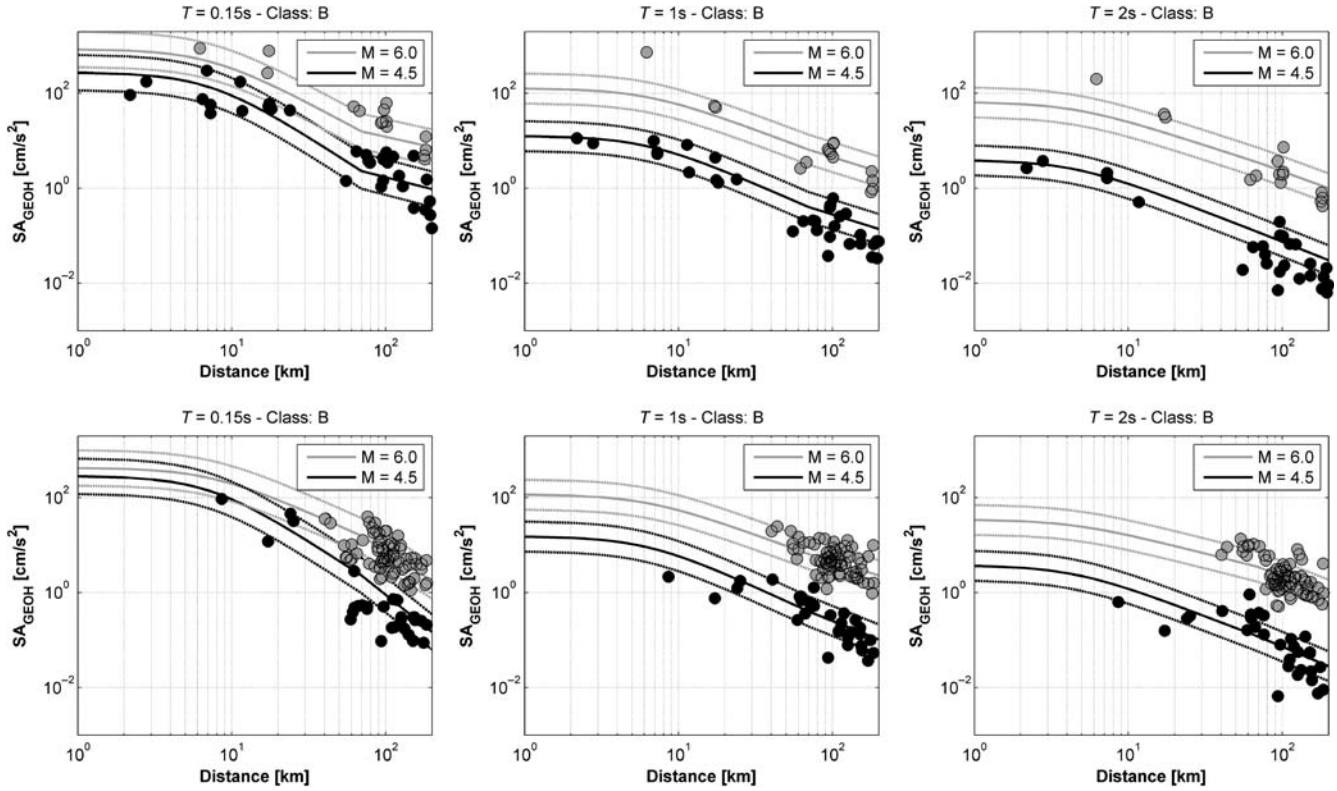

Figure 9. Comparison between predicted and observed spectral acceleration for EC8 B sites at low (M 4.5 $\pm$ 0.3) and moderate magnitudes (M 6.0 $\pm$ 0.3). (Left column) $T = 0.15$ s; (central column) $T = 1$ s; (right column) $T = 2$ s. (Top row) PEA; (bottom row) NA.

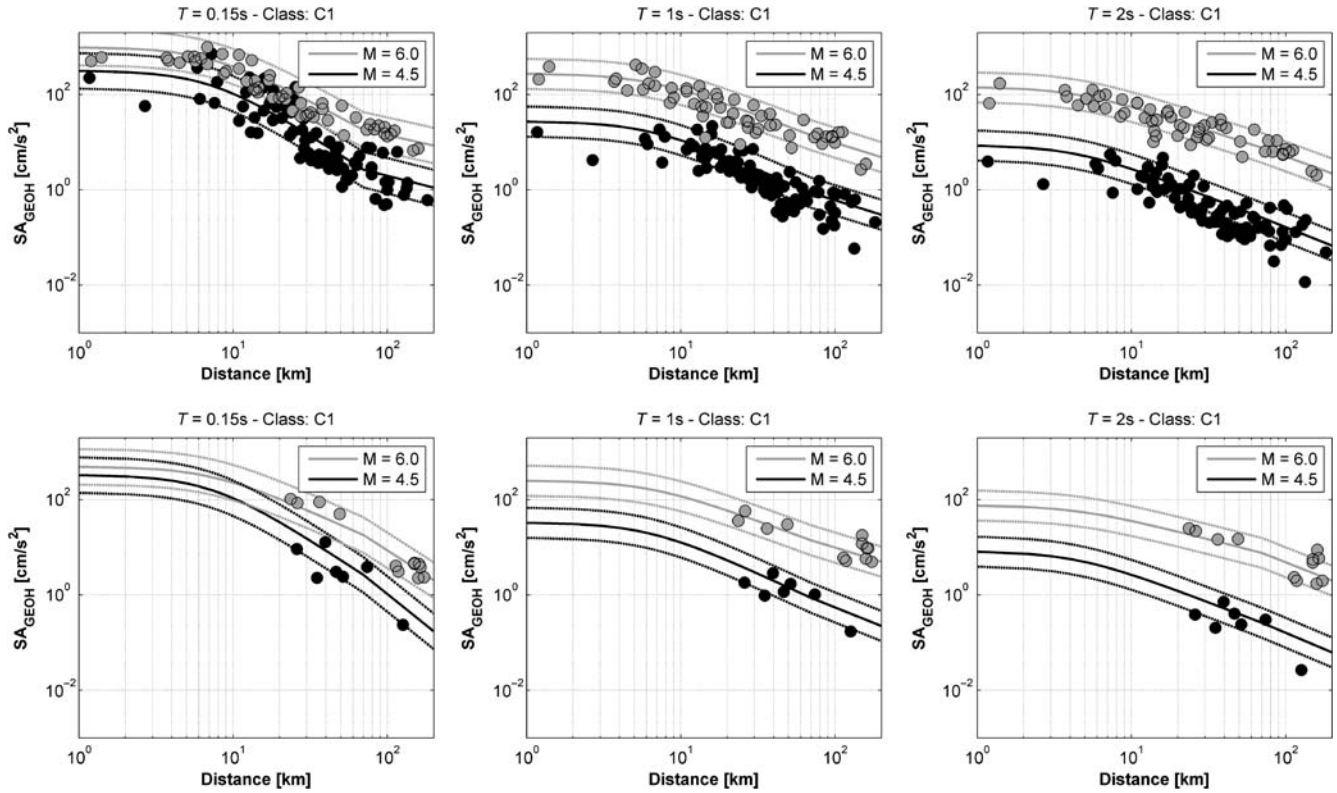

Figure 10. Comparison between predicted and observed spectral acceleration for EC8 C sites inside basins (C1) at low (M 4.5 $\pm$ 0.3) and moderate magnitudes (M 6.0 $\pm$ 0.3). (Left column) $T = 0.15$ s; (middle column) $T = 1$ s; (right column) $T = 2$ s. (Top row) PEA; (bottom row) NA.

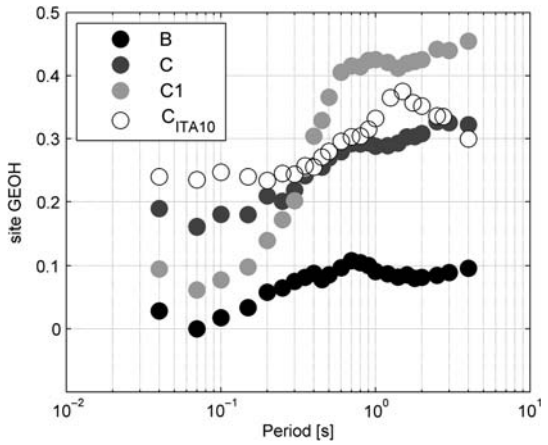

Figure 11. Site coefficients s_B (black circles), s_C (dark gray circles), and s_C corrected for F_{bas} (light gray circles), obtained from the regression of the geometrical mean of the horizontal components. White circles are ITA10 class C coefficients.

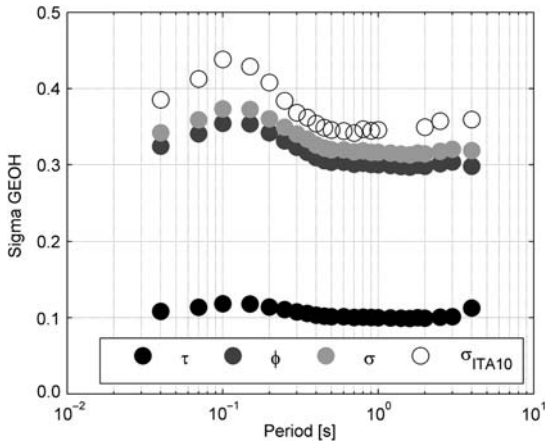

Figure 12. NI15 period-dependent standard deviation of total (σ), between-event (τ), and within-event (ϕ) residuals. White circles are the DBNI total variability estimated from ITA10 (σ_{ITA10}).

We obtained the magnitude–distance–deaggregation ($M-R-\varepsilon$) distribution resulting from the deaggregation of the hazard at the two sites, considering the 10% of exceedance in 50 years ($T_r \sim 475$ yrs) for PGA and psuedospectral acceleration (PSA; $T = 0.15$, 1, and 2 s). In this way, we obtain the modal values of magnitude from the $M-R-\varepsilon$ distribution for the two sites (M 5.0 for site S1 and M 4.7 for site S2), to show the differences of the median estimates and standard deviation between ITA10 and NI15 at those magnitudes (Figs. 15 and 16 for sites S1 and S2, respectively).

The major differences in the attenuation curves are observed at both sites at short periods (PGA and $T = 0.15$ s) and distance ranges 10–70 km (NI15 lower than ITA10) and 100–200 km (NI15 higher than ITA10). At longer periods

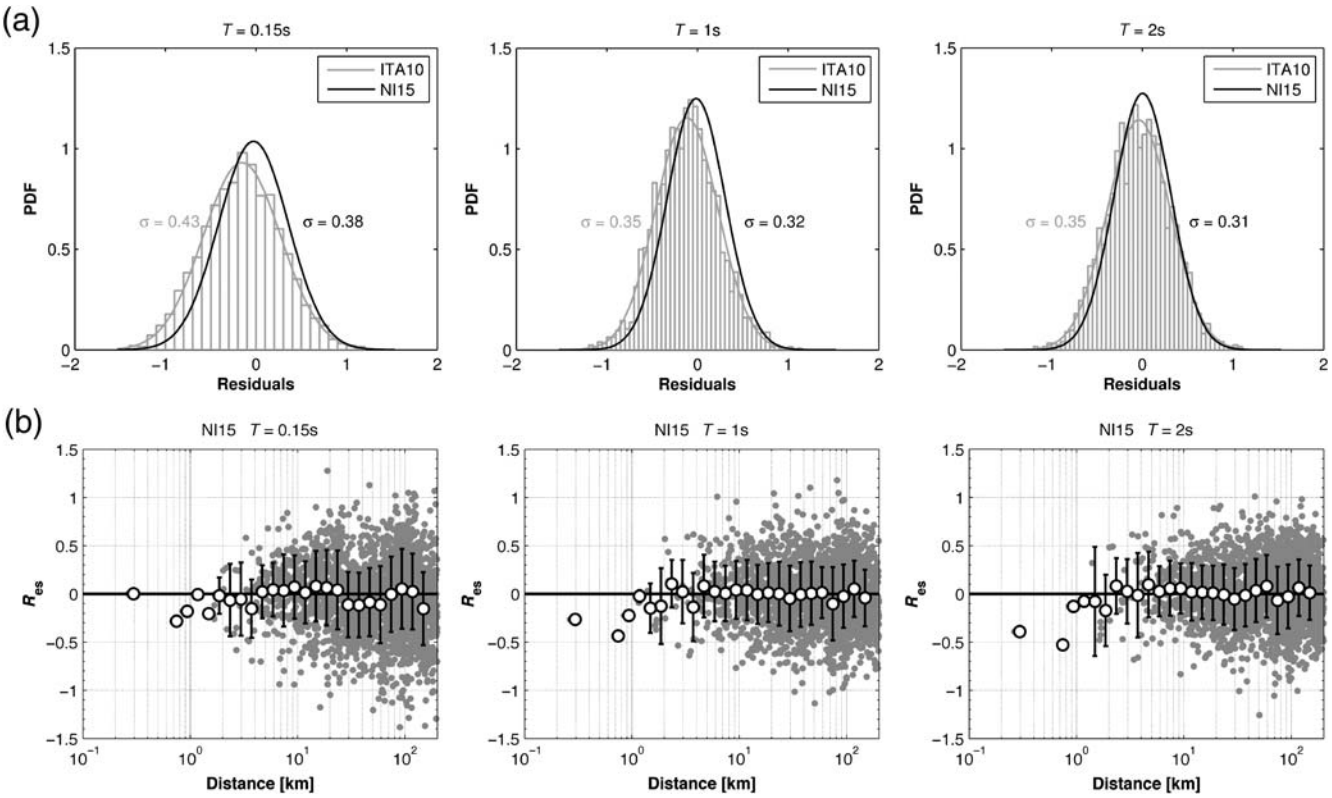

Figure 13. Distributions of NI15 residuals at 0.15, 1, and 2 s: (a) histograms and probability density functions (PDFs) of DBNI residuals estimated from ITA10 (gray) superimposed on the NI15 PDF (black); (b) NI15 total residuals versus distance. White dots and black bars represent the mean and standard deviation of the residuals for each distance bin, respectively.

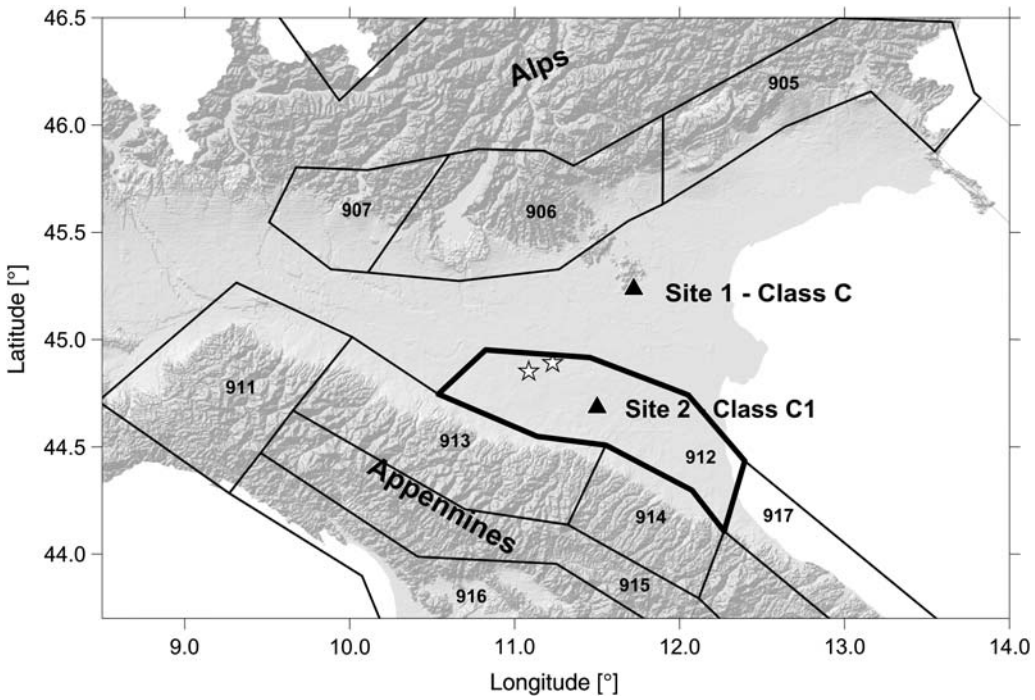

Figure 14. Map of the seismic sources zone model (Meletti *et al.*, 2008) of northern Italy. White stars represent the mainshocks of the 2012 Emilia sequence; black triangles are the two sites selected for probabilistic seismic-hazard assessment.

($T = 1$ and 2 s), the major differences are observed at distances larger than 50 km (NI15 lower than ITA10) for both sites (Figs. 15 and 16 for sites S1 and S2, respectively).

The consequence for site S1 is that the hazard curves obtained using NI15 are lower than the ones generated using ITA10 in the entire range of the annual rate of exceedance. In particular, for SA at 1 s, the largest reduction is about 64% for 10% probability of exceedance in 50 yrs (return period of about 475 yrs) and 67% for 2% probability of exceedance in 50 yrs (return period of about 2475 yrs).

On the contrary, site S2 shows slighter reduction at short periods; and, at long periods, the hazard values are very similar using either NI15 or ITA10. The results of the hazard calculation for the selected IMs at the two probabilities of exceedance are shown in Table 7.

Discussion and Conclusions

In this study, we explore how local GMPEs can significantly improve the median estimates of ground motion and

Table 6
Data Input for Probabilistic Seismic-Hazard Analysis (PSHA) Calculation

AS	β	$\Sigma(\beta)$	M_{max}	M_{max} Uncertainty	Total Annual Rate, λ (Events/Year; $M \geq 4.76$)	AS Depth (km)	FM
905	2.48	0.37	6.6	0.19	0.33	8	RF
906	2.86	0.69	6.6	0.19	0.13	8	RF
907	4.18	1.49	6.14	0.19	0.06	8	RF
911	3.72	1.11	6.14	0.19	0.05	7	SS
912*	3.09	0.58	6.14	0.19	0.10	7	RF
913	4.13	0.44	6.14	0.19	0.20	7	UN
914	3.07	0.29	6.14	0.19	0.18	5	UN
915	3.33	0.41	6.6	0.19	0.05	7	NF
916	4.50	0.71	6.14	0.19	0.09	9	NF

AS, ZS9 seismic source code; β, natural logarithm of the relative likelihood of large and small earthquakes in the Gutenberg–Richter recurrence law ($\beta = \ln(b)$); $\Sigma(\beta)$, standard error associated with the β coefficient; M_{max}, maximum magnitude for each zone; M_{max} uncertainty, uncertainty associated with maximum magnitude; λ, total occurrence earthquake rates; AS depth, average event depths for each AS; FM, prevalent style of faulting of each AS (RF, reverse fault; SS, strike slip; UN, undefined; NF, normal fault).

*Zone includes the epicentral area of the 2012 Emilia seismic sequence.

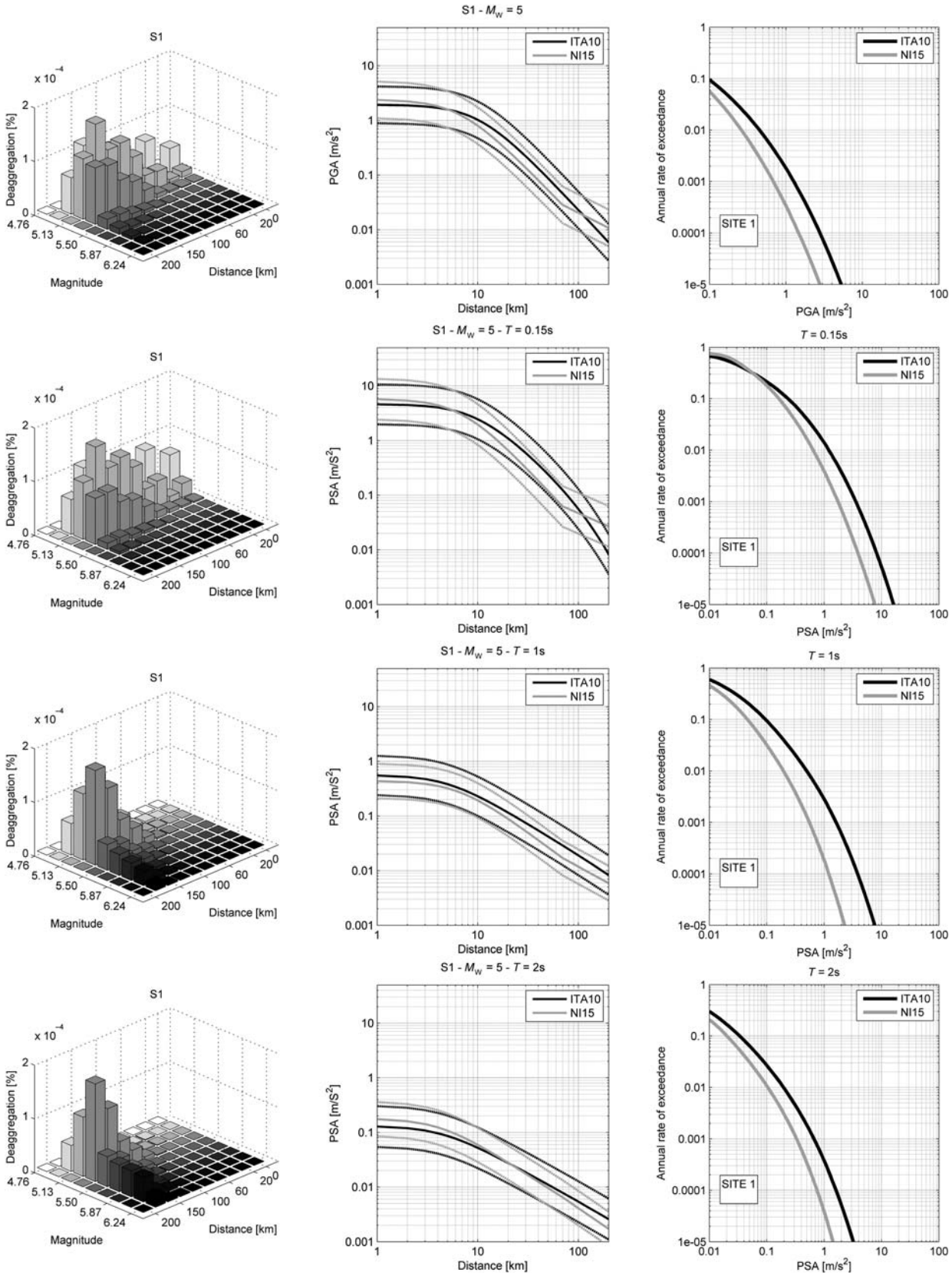

Figure 15. Probabilistic seismic hazard at site S1 for PGA and pseudospectral acceleration (PSA; $T = 0.15$, 1, and 2 s). (Left column) joint magnitude–distance–deaggregation ($M-R-\varepsilon$) distributions resulting from disaggregation of the selected parameters; (middle column) ground-motion models for the modal value of magnitudes of $M-R-\varepsilon$ distributions; (right column) annual rate of exceedance of intensity measures (IMs; black lines indicate ITA10 and gray lines NI15).

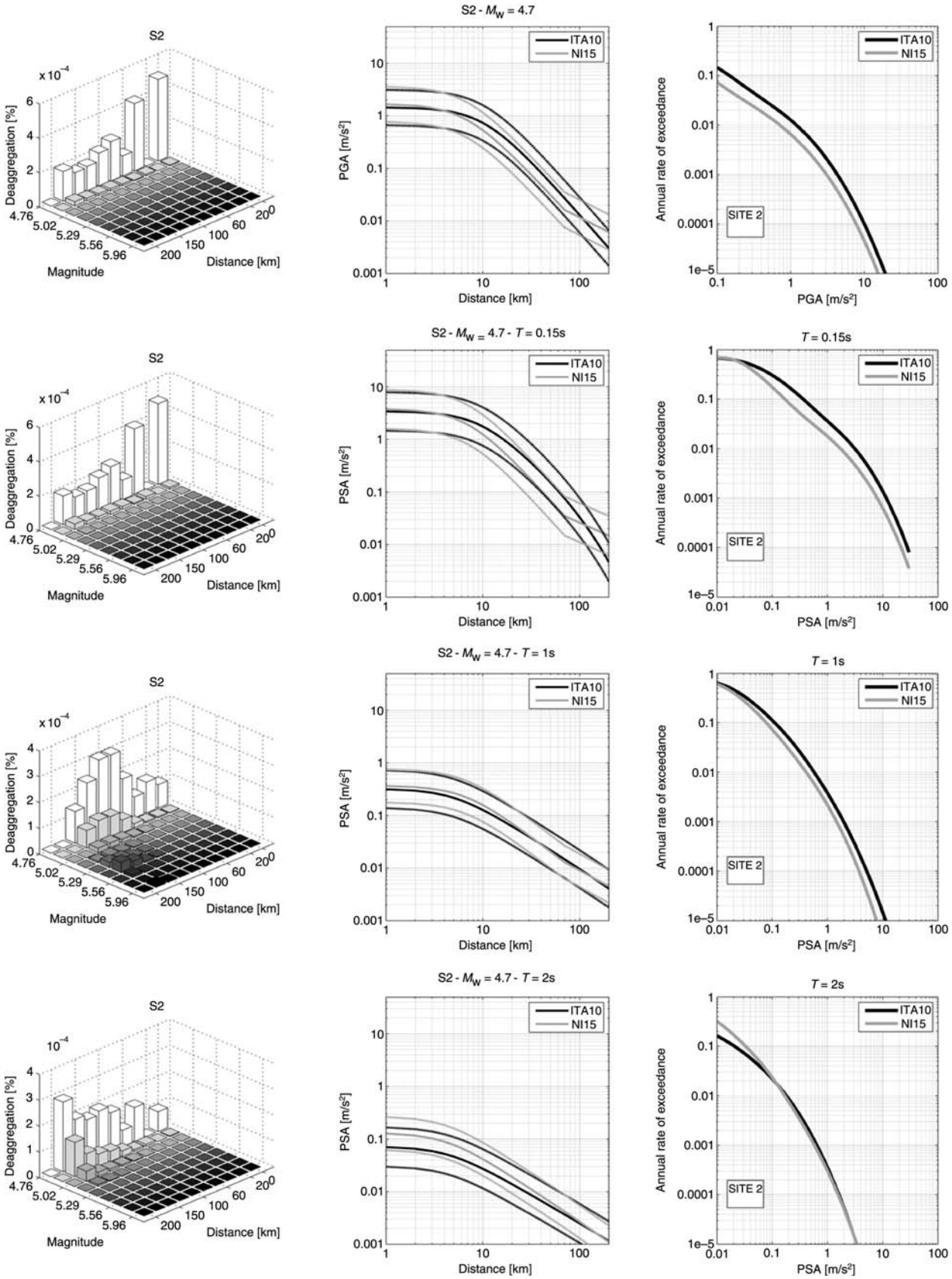

Figure 16. Probabilistic seismic hazard at site S2 for PGA and PSA ($T = 0.15$, 1, and 2 s). (Left column) joint $M-R-\varepsilon$ distributions resulting from disaggregation of the selected parameters; (central column) ground-motion models for the modal value of magnitudes of $M-R-\varepsilon$ distributions; (right column) annual rate of exceedance of IMs (black lines indicate ITA10 and gray lines NI15).

Table 7
PSHA Values of PGA and Spectral Ordinates ($T = 0.15$, 1, and 2 s) for the Selected Sites at Probability of Exceedance $P = 10\%$ and $P = 2\%$ in 50 yrs.

	Site S1				Site S2			
	$P = 10\%$ in 50 yrs		$P = 2\%$ in 50 yrs		$P = 10\%$ in 50 yrs		$P = 2\%$ in 50 yrs	
IMs (cm/s^2)	ITA10	NI15	ITA10	NI15	ITA10	NI15	ITA10	NI15
PGA	93.3	51.6	184	93.3	305	218	601	466
$T = 0.15$ s	258	131	507	237	843	552	1660	1290
$T = 1$ s	111	40	237	78.8	142	102	305	218
$T = 2$ s	47.4	24.1	102	47.4	47.4	40	93.3	85.8

IM, intensity measure; ITA10, Bindi *et al.* (2011) model; NI15, (this study) northern Italy model.

reduce the variability of the expected seismic shaking and consequently influence the assessment of the probabilistic seismic hazard. We investigate the peculiar propagation effects and site response of northern Italy, which includes a large alluvial basin (Po Plain) representative of the setting of large urban areas exposed to high seismic risk.

We examine the applicability of existing ground-motion models in this area and show that they cannot adequately represent the complexity of the local physical phenomena related to wave propagation (phase reflections, generation of surface waves, or site effects). We select and rank a list of existing models (regional, pan-European, or global) using the LLH approach (Delavaud *et al.*, 2009; Scherbaum *et al.*, 2009). We find that the best performing model is the one proposed by Bindi *et al.* (2011) for the Italian territory, although it does not adequately fit the observations in the 30–100 km distance range at short periods (<0.3 s) and in the 10–30 km range at long periods (>2 s). The analysis of the recordings shows that there is a different wave attenuation in the PEA and NA, especially at short periods (due to the *SmS* reflections from the Moho discontinuity in PEA), and a strong amplification of the horizontal and vertical components of ground motion at long periods (>2 s).

We derive a new set of GMPEs (referred to as NI15), including, in the functional form used by Bindi *et al.* (2011), additional factors controlling the ground motion in the area, in particular different geometrical attenuation for PEA and NA, as well as basin effects due to the presence of thick sedimentary cover.

The derived GMPEs supersede the existing local model (Massa *et al.*, 2008), derived from a limited number of data and poor quality of metadata. In addition, there is both an improvement of the median estimates and the reduction of about 10% of the standard deviation of the residuals with respect to Bindi *et al.* (2011).

This tailored model has a relevant impact on the hazard evaluation for the area and, in particular, for the sites located in the background area of the reference Italian seismic zonation for the hazard assessment (ZS9, Meletti *et al.*, 2008). The largest hazard reduction is found for SA at 1 s and is about 64% and 67% for 10% and 2% probability of exceedance in 50 yrs, respectively. Sites located within the seismogenic zones show slighter reduction both at short and long periods.

As in PSHA, in which different GMPEs can be applied in different branches of the logic tree (Scherbaum *et al.*, 2005; Scherbaum, and Kuehn, 2011; Musson, 2012), we propose consideration of NI15 for source areas located within the area covered by the database (northern Italy), similar to the local GMPEs for volcanic areas adopted in the Italian hazard map.

As a further development, the obtained improvement in the median prediction can be coupled with single-station sigma models, moving toward partially nonergodic hazard assessment (Faccioli *et al.*, 2015).

Data and Resources

The Italian strong-motion data and the geologic and geotechnical information regarding the strong-motion stations of the target area were searched using the ITalian ACcelerometric Archive, ITACA 2.0 (http://itaca.mi.ingv.it, last accessed April 2015). All information on the SeIsmic Ground Motion Assessment (SIGMA) project can be found at http://www.projet-sigma.com/ (last accessed August 2015). Data for the hazard map of Italy can be found at http://zonesismiche.mi.ingv.it (last accessed April 2015). Data from the Catalogo Parametrico dei Terremoti Italiani (Gruppo di Lavoro CPTI 2004) are available at http://emidius.mi.ingv.it/CPTI04 (last accessed April 2015). The code for seismic-hazard assessment is CRISIS 2015, by Universidad Nacional Autonoma de México.

Acknowledgments

This work has been partially funded by the SeIsmic Ground Motion Assessment (SIGMA) project. The authors are grateful to John Douglas for his helpful suggestions, which improved the quality of this research, and thank Marco Santulin (Istituto Nazionale di Geofisica e Vulcanologia [INGV], Milano), Carlo Meletti (INGV, Pisa) and the CRISIS Working Group for kindly providing the software CRISIS 2015.

References

Abrahamson, N. A., and R. R. Youngs (1992). A stable algorithm for regression analysis using the random effects model, *Bull. Seismol. Soc. Am.* **82,** 505–510.

Akkar, S., and J. J. Bommer (2010). Empirical equations for the prediction of PGA, PGV, and spectral accelerations in Europe, the Mediterranean region, and the Middle East, *Seismol. Res. Lett.* **81,** no. 2, 195–206.

Akkar, S., M. A. Sandıkkaya, M. Senyurt, A. Azari Sisi, B. Ö. Ay, P. Traversa, J. Douglas, F. Cotton, L. Luzi, B. Hernandez, *et al.* (2013). Reference database for seismic ground-motion in Europe (RESORCE), *Bull. Earthq. Eng.* **12,** no. 1, 311–339.

Al Atik, L., N. Abrahamson, J. J. Bommer, F. Scherbaum, F. Cotton, and N. Kuehn (2010). The variability of ground-motion prediction models and its components, *Seismol. Res. Lett.* **81,** no. 5, 794–801.

Atkinson, G., and D. Boore (2011). Modifications to existing ground-motion prediction equations in light of new data, *Bull. Seismol. Soc. Am.* **101,** 1121–1135.

Beauval, C., H. Tasan, A. Laurendeau, E. Delavaud, F. Cotton, P. Guéguen, and N. Kuehn (2012). On the testing of ground-motion prediction equations against small-magnitude data, *Bull. Seismol. Soc. Am.* **102,** 1994–2007.

Bindi, D., M. Massa, L. Luzi, G. Ameri, F. Pacor, R. Puglia, and P. Augliera (2014). Pan-European ground-motion prediction equations for the average horizontal component of PGA, PGV and 5%-damped PSA at spectral periods up to 3.0 s using the RESORCE dataset, *Bull. Earthq. Eng.* **12,** 391–430.

Bindi, D., F. Pacor, L. Luzi, R. Puglia, M. Massa, G. Ameri, and R. Paolucci (2011). Ground motion prediction equations derived from the Italian strong motion database, *Bull. Earthq. Eng.* **9,** 1899–1920.

Boore, D. M., J. P. Stewart, E. Seyan, and G. M. Atkinson (2014). NGA-West2 equations for predicting PGA, and 5% damped PSA for shallow crustal earthquakes, *Earthq. Spectra* **30,** no. 3, 1057–1085.

Bordoni, P., R. M. Azzara, F. Cara, R. Cogliano, G. Cultrera, G. Di Giulio, A. Fodarella, G. Milana, S. Pucillo, G. Riccio, *et al.* (2012). Preliminary results from EMERSITO, a rapid response network for site-effect studies, in *The Emilia (Northern Italy) Seismic Sequence of May–June, 2012: Preliminary Data and Results*, M. Anzidei, A. Maramai, and P. Montone (Editors), special issue, *Ann. Geophys.* 55, no. 4, 599–607.

Bradley, B. A. (2013). A New Zealand-specific pseudospectral acceleration ground-motion prediction equation for active shallow crustal earthquakes based on foreign models, *Bull. Seismol. Soc. Am.* **103,** no. 3, 1801–1822.

Bragato, P. L., M. Sugan, P. Augliera, M. Massa, A. Vuan, and A. Sarao (2011). Moho reflection effects in the Po Plain (northern Italy) observed from instrumental and intensity data, *Bull. Seismol. Soc. Am.* **10,** no. 5, 2142–2152.

Campbell, K. W., and Y. Bozorgnia (2014). NGA-West2 ground motion model for the average horizontal components of PGA, PGV, and 5% damped linear acceleration response spectra, *Earthq. Spectra* **30,** no. 3, 1087–1115, doi: 10.1193/062913EQS175M.

Cassano, E., L. Anelli, R. Fichera, and V. Cappelli (1986). Po Plain: Integrated interpretation of geophysical and geological data, *73th Conference of Italian Geological Society*, Rome, Italy, 29 September–4 October (in Italian).

Castro, R. R., F. Pacor, R. Puglia, G. Ameri, J. Letort, M. Massa, and L. Luzi (2013). The 2012 May 20 and 29, Emilia earthquakes (northern Italy) and the main aftershocks: S-wave attenuation, acceleration source functions and site effects, *Geophys. J. Int.* **195,** 597–611.

Cauzzi, C., and E. Faccioli (2008). Broadband (0.05 to 20 s) prediction of displacement response spectra based on worldwide digital records, *J. Seismol.* **12,** no. 4, 453–475.

Cauzzi, C., E. Faccioli, M. Vanini, and A. Bianchini (2014). Updated predictive equations for broadband (0.01–10 s) horizontal response spectra and peak ground motions, based on a global dataset of digital acceleration records, *Bull. Earthq. Eng.* **13,** doi: 10.1007/s10518-014-9685-y.

de Nardis, R., L. Filippi, G. Costa, P. Suhadolc, M. Nicoletti, and G. Lavecchia (2014). Strong motion recorded during the Emilia 2012 thrust earthquakes (northern Italy): A comprehensive analysis, *Bull. Earthq. Eng.* **12,** no. 5, 2117–2145.

Delavaud, E., F. Scherbaum, N. Kuehn, and C. Riggelsen (2009). Information-theoretic selection of ground-motion prediction equations for seismic hazard analysis: An applicability study using Californian data, *Bull. Seismol. Soc. Am.* **99,** 3248–3263.

Di Capua, G., G. Lanzo, V. Pessina, S. Peppoloni, and G. Scasserra (2011). The recording stations of the Italian strong motion network: Geological information and site classification, *Bull. Earthq. Eng.* **9,** 1779–1796.

Douglas, J., P. Suhadolc, and G. Costa (2004). On the incorporation of the effect of crustal structure into empirical strong ground motion estimation, *Bull. Earthq. Eng.* **2,** 75–99.

Eurocode 8 (2004). Design of structures for earthquake resistance, Part 1: General rules, seismic actions and rules for buildings, EN 1998-1, European Committee for Standardization (CEN), Brussels, http://www.cen.eu/cenorm/homepage.htm (last accessed April 2014).

Faccioli, E., R. Paolucci, and M. Vanini (2015). Evaluation of Probabilistic Site-Specific seismic-hazard methods and associated uncertainties, with applications in the Po Plain, Northern Italy, *Bull. Seismol. Soc. Am.* **105,** no. 5, 2787–2807.

Faenza, L., and A. Michelini (2010). Regression analysis of MCS intensity and ground motion parameters in Italy and its application in ShakeMap, *Geophys. J. Int.* **180,** no. 3, 1138–1152.

Lin, P. S., B. Chiou, N. Abrahamson, M. Walling, C. T. Lee, and C. T. Cheng (2011). Repeatable source, site, and path effects on the standard deviation for empirical ground-motion prediction models, *Bull. Seismol. Soc. Am.* **101,** no. 5, 2281–2295.

Luzi, L., S. Hailemikael, D. Bindi, F. Pacor, F. Mele, and F. Sabetta (2008). ITACA (Italian ACcelerometric Archive): A web portal for the dissemination of Italian strong-motion data, *Seismol. Res. Lett.* **79,** no. 5, 716–722.

Luzi, L., F. Pacor, G. Ameri, R. Puglia, P. Burrato, M. Massa, P. Augliera, G. Franceschina, S. Lovati, and R. Castro (2013). Overview on the strong-motion data recorded during the May–June 2012 Emilia seismic sequence, *Seismol. Res. Lett.* **84,** 629–644.

Massa, M., P. Morasca, L. Moratto, S. Marzorati, G. Costa, and D. Spallarossa (2008). Empirical ground-motion prediction equations for northern Italy using weak- and strong-motion amplitudes, frequency content, and duration parameters, *Bull. Seismol. Soc. Am.* **98,** 1319–1342.

Meletti, C., V. D'Amico, G. Ameri, A. Rovida, and M. Stucchi (2012). Seismic hazard in the Po Plain and the 2012 Emilia earthquakes, *Ann. Geophys.* **55,** no. 4, 623–629.

Meletti, C., F. Galadini, G. Valensise, M. Stucchi, R. Basili, S. Barba, G. Vannucci, and E. Boschi (2008). A seismic source zone model for the seismic hazard assessment of the Italian territory, *Tectonophysics* **450,** no. 1, 85–108.

Morikawa, N., T. Kanno, A. Narita, H. Fujiwara, T. Okumura, Y. Fukushima, and A. Guerpinar (2008). Strong motion uncertainty determined from observed records by dense network in Japan, *J. Seismol.* **12,** no. 4, 529–546.

Musson, R. (2012). On the nature of logic trees in probabilistic seismic hazard assessment, *Earthq. Spectra* **28,** 1291–1296.

Ordaz, M., F. Martinelli, V. D'Amico, and C. Meletti (2013). CRISIS2008: A flexible tool to perform probabilistic seismic hazard assessment, *Seismol. Res. Lett.* **84,** no. 3, 495–504.

Pacor, F., L. Luzi, M. Massa, and D. Bindi (2012). Ranking of available GMPEs from residual analysis for northern Italy and definition of reference GMPEs, *SIGMA Project, Deliverable SIGMA-2012-D2-53-02*, http://projet-sigma.com/index.html (last accessed April 2015).

Pacor, F., R. Paolucci, L. Luzi, F. Sabetta, A. Spinelli, A. Gorini, M. Nicoletti, S. Marcucci, L. Filippi, and M. Dolce (2011). Overview of the Italian strong motion database ITACA 1.0, *Bull. Earthq. Eng.* **9,** no. 6, 1723–1739.

Paolucci, R., F. Pacor, R. Puglia, G. Ameri, C. Cauzzi, and M. Massa (2011). Record processing in ITACA, the new Italian strong motion database, in *Earthquake Data in Engineering Seismology, Geotechnical, Geological and Earthquake Engineering Series*, S. Akkar, P. Gulkan, and T. Van Eck (Editors), Vol. 14, no. 8, Springer, Berlin, 99–113.

Scherbaum, F., and N. M. Kuehn (2011). Logic tree branch weights and probabilities: Summing up to one is not enough, *Earthq. Spectra* **27,** 1237–1251.

Scherbaum, F., J. J. Bommer, H. Bungum, F. Cotton, and N. A. Abrahamson (2005). Composite ground-motion models and logic-trees: Methodology, sensitivities and uncertainties, *Bull. Seismol. Soc. Am.* **95,** 1575–1593.

Scherbaum, F., E. Delavaud, and C. Riggelsen (2009). Model selection in seismic hazard analysis: An information-theoretic perspective, *Bull. Seismol. Soc. Am.* **99,** 3234–3247.

Seyhan, E., J. P. Stewart, T. D. Ancheta, R. B. Darragh, and R. W. Graves (2014). NGA-West2 site database, *Earthq. Spectra* **30,** no. 3, 1007–1023.

Stucchi, M., C. Meletti, V. Montaldo, H. Crowley, G. M. Calvi, and E. Boschi (2011). Seismic hazard assessment (2003–2009) for the Italian Building Code, *Bull. Seismol. Soc. Am.* **101,** no. 4, 1885–1911.

Istituto Nazionale di Geofisica e Vulcanologia
Sezione di Milano
Via Corti 12
20133 Milano
Italy
giovanni.lanzano@ingv.it
(G.L., M.D., R.P., L.L., F.P.)

Istituto di Geologia Ambientale e Geoingegneria
Consiglio Nazionale delle Ricerche Area della Ricerca di Roma 1, Montelibretti
Via Salaria km 29,3
Montorotondo, Italy
(C.F.)

Deutsches GeoforschungsZentrum
Telegrafenberg
14473 Potsdam
Germany
(D.B.)

Manuscript received 7 November 2015;
Published Online 12 January 2016